

Theoretical and experimental investigation of the equation of state of boron plasmas

Shuai Zhang,^{1,*} Burkhard Militzer,^{2,3,†} Michelle C. Gregor,^{1,‡} Kyle Caspersen,¹ Lin H. Yang,¹ Tadashi Ogitsu,¹ Damian Swift,¹ Amy Lazicki,¹ D. Erskine,¹ Richard A. London,¹ P. M. Celliers,¹ Joseph Nilsen,¹ Philip A. Sterne,¹ and Heather D. Whitley^{1,§}

¹*Lawrence Livermore National Laboratory, Livermore, California 94550, USA*

²*Department of Earth and Planetary Science, University of California, Berkeley, California 94720, USA*

³*Department of Astronomy, University of California, Berkeley, California 94720, USA*

(Dated: February 24, 2022)

We report a theoretical equation of state (EOS) table for boron across a wide range of temperatures (5.1×10^4 – 5.2×10^8 K) and densities (0.25 – 49 g/cm³), and experimental shock Hugoniot data at unprecedented high pressures (5608 ± 118 GPa). The calculations are performed with full, first-principles methods combining path integral Monte Carlo (PIMC) at high temperatures and density functional theory molecular dynamics (DFT-MD) methods at lower temperatures. PIMC and DFT-MD cross-validate each other by providing coherent EOS (difference < 1.5 Hartree/boron in energy and $< 5\%$ in pressure) at 5.1×10^5 K. The Hugoniot measurement is conducted at the National Ignition Facility using a planar shock platform. The pressure-density relation found in our shock experiment is on top of the shock Hugoniot profile predicted with our first-principles EOS and a semi-empirical EOS table (LEOS 50). We investigate the self diffusivity and the effect of thermal and pressure-driven ionization on the EOS and shock compression behavior in high pressure and temperature conditions. We study the performance sensitivity of a polar direct-drive exploding pusher platform to pressure variations based on comparison of the first-principles calculations with LEOS 50 via 1D hydrodynamic simulations. The results are valuable for future theoretical and experimental studies and engineering design in high energy density research. (LLNL-JRNL-748227)

I. INTRODUCTION

Recent experiments at the National Ignition Facility (NIF) have demonstrated the utility of large diameter polar direct-drive exploding pushers (PDXP) as a low areal density platform for nucleosynthesis experiments,[1] neutron source development, neutron and x-ray diagnostic calibration, and potentially as a candidate platform for heat transport studies.[2] Improving the platform for each of these respective uses requires consideration of various model uncertainties. Achieving a lower shell areal density during burn or obtaining additional data to help constrain estimates of this quantity in the nucleosynthesis experiments would simplify analysis of the charged particle data collected, while improving implosion symmetry is a necessary requirement if the platform is to be used to study heat transport. Variations in the ablators used in these experiments is one possible avenue that is currently under investigation. The use of glow-discharge polymer (GDP) as an ablator improves performance over smaller glass capsules,[1] but its low tensile strength requires designs with shell thickness of about 15–20 μm in order to support gas fill pressures of around 8 bar. Higher tensile strength materials offer the option of producing thinner shells to support similar fill pressures, and reactions of ablator materials with neutrons and protons could potentially be used to obtain additional data

to help quantify shell areal density at burn time. Some candidate materials with higher tensile strength include beryllium, boron, boron carbide, boron nitride, and high density carbon. For the purpose of conducting heat flow measurements, beryllium was ruled out as a candidate material due to the inclusion of argon within the capsule during the fabrication process.[2] Boron and nitrogen, which both undergo reactions with neutrons and protons, offer the potential for using additional nuclear reactions to better constrain the shell areal density during nuclear burn time, which could improve our overall understanding of the effects of the shell on the measured charged particles in the nucleosynthesis experiments. Boron is also interesting as an ablator material since its reactions with γ -rays could be used to constrain ablator mix at burn time.[3]

Radiation hydrodynamic simulations are the workhorse method for design and analysis of the inertial confinement fusion (ICF) and high energy density experiments. It has been demonstrated in many previous studies that the equation of state (EOS) of capsule ablator materials is an important component in indirect drive ICF performance,[4–8] and EOS may also affect the implosion dynamics in the polar direct-drive platform, impacting not only capsule yield, but also the shell areal density during burn and the electron-ion temperature separation in the gas. Thus, exploration of these materials as candidates for future PDXP-based experiments requires reasonable EOS models for use in radiation hydrodynamic simulations. In this paper, we examine the EOS of boron via both *ab initio* simulations and experimental measurements. We also examine its performance as an ablator in 1D simulations of the

* zhang49@llnl.gov

† militzer@berkeley.edu

‡ gregor3@llnl.gov

§ whitley3@llnl.gov

PDXP platform, focusing on how variations in the EOS impact the computed yield and plasma conditions at burn time.

EOS models that are widely used in hydrodynamic simulation codes, such as the quotidian EOS (QEOS) [9, 10], provide pressures and energies as smooth functions of temperature and density based on semi-empirical methods, such as the Thomas-Fermi (TF) theory. The TF theory treats the plasma as a collection of nuclei that follow Boltzmann statistics and electrons that form continuous fluids and obey Fermi-Dirac statistics. This offers a good means to describe weakly-coupled plasmas and materials at very high densities, but is insufficient in describing many condensed matter solids and liquids, where bonding effects are significant. Additionally, at low-to-intermediate temperatures where atoms undergo partial ionization, the TF theory does not accurately capture the effects of shell ionization, which impacts the electronic contribution to the EOS of the material.

There has been continuous research in the development of improved methods for computing thermodynamic properties of materials, which has resulted in a variety of methods that can be applied to study EOS across a wide range of densities and temperatures. Methods appropriate to the study of plasmas include density functional theory (DFT)-based methods such as INFERN0 [11], Purgatorio [12, 13], orbital-free (OF) quantum molecular dynamics (MD) [14, 15], and extended-DFT [16], activity-expansion method (ACTEX) [17–19], and many-body path integral Monte Carlo (PIMC) [20–24] methods. Standard Kohn-Sham DFT-MD has been widely applied for EOS studies of condensed matter as well as warm and hot, dense plasmas. It accounts for both the electronic shells and bonding effects, and is thus superior to average-atom methods in situations where these types of strong many-body correlations are impactful to the EOS. However, the DFT-MD approach becomes computationally intractable at high temperatures because considerable numbers of partially occupied orbitals need to be considered.

As a powerful tool initially developed for hydrogen [25], PIMC has been successfully utilized to study plasmas from weak coupling to strongly coupled regimes with high accuracy. Recent developments by Militzer et al. [24, 26] provide useful recipes for studying higher-Z plasmas. In the past seven years, they have implemented the PIMC methods under the fixed-node approximation and obtained the EOS for a series of elements (C, N, O, Ne, Na, Si) [24, 26–31] and compounds (H_2O , LiF, hydrocarbons) [26, 32–34] over a wide range of temperature, pressure conditions. The goal of the theoretical part of this paper is to apply these methods to calculate the EOS of boron, and explore the effect on PDXP simulations in comparison with an older EOS model (LEOS 50) through hydrodynamic simulations.

Located in between metals and insulators in the periodic table, the structure and properties of boron have attracted wide interest in high pressure physics. A num-

ber of studies have examined the stability relations of the α and the β phases [35–37]. A phase diagram was proposed for crystalline boron based on DFT simulations [38], showing five different phases at pressures up to 300 GPa, part of which having been confirmed in static compression experiments using diamond anvil cells. A considerable amount of study has been performed on boron at low densities, including DFT-MD simulations and X-ray radiography measurements on the structure, electronic, and thermodynamic properties of liquid boron [39–41], general chemical models for the the composition and transport properties of weakly-coupled boron plasmas [42], isochoric EOS and resistivity of warm boron by combining closed vessel experiments, DFT-MD, average-atom methods, and a chemical model (COMPTRA) [43–48]. In comparison to the vast progress in the low-temperature, high-pressure and the high-temperature, low-pressure regions of the boron phase diagram, studies at simultaneously high pressures and temperatures are rare. Until the year 2013, the only shock Hugoniot data available were at pressures below 112 GPa [49]. Recently, Le Pape et al. [50] used X-ray radiography to study the structure of shocked boron. They reported two experimental Hugoniot measurements and ion-ion structure factors that are consistent with DFT-MD simulations. This extended the shock Hugoniot measurements of boron to the highest pressure of 400 GPa.

Hydrodynamic simulations of PDXP experiments require the EOS of the ablator materials along and off the Hugoniot curve at higher temperatures and pressures. The LEOS [9, 10] and SESAME [51] EOS databases may be used, but it is unclear how their deviation from the true values affect the reliability of results in PDXP simulations, such as the neutron yield. In this work, we perform calculations of the boron EOS over a wide range of temperatures and pressures. We extend PIMC simulations of dense boron plasmas from the “hot” down to the “warm” region, where significant partial ionization of the K shell persists and standard DFT-MD simulations with frozen 1s core pseudopotentials are not trustworthy. At relatively low temperatures, the system behaves like the usual condensed matter fluid, which can be reasonably well described within the DFT-MD framework. By pushing PIMC to low temperatures and DFT-MD to high temperatures, we get a coherent, first-principles EOS table for boron. We compare this table and the predicted shock compression profiles with LEOS and SESAME EOS tables for boron, and perform hydrodynamic simulations to compare the effect of the different tables on the ICF performance.

The paper is organized as follows: Section II introduces the details of our simulation methods and experiment. Sec. III presents our EOS results, the calculated and measured shock Hugoniot data, and comparisons with other theories and models. Sec. IV discusses the atomic and electronic properties of boron plasmas, the ionization process, and PDXP performance sensitive to the EOS; finally we conclude in Sec. V.

II. THEORY AND EXPERIMENT

A. First-principles simulation methods

Following the pioneering work applying PIMC to the simulations of real materials (hydrogen) [25] and recent development for pure carbon [26], hydrocarbons [33, 34], and lithium in LiF [32], our PIMC simulations [52] utilize the fixed-node approximation [53] and treat both electrons and the nuclei as quantum paths that are cyclic in imaginary time $[0, \beta=1/k_B T]$, where k_B is the Boltzmann constant. We use free-particle nodes to constrain the path to positive regions of the trial density matrix, which has been shown to work well for calculations of hydrogen [25, 54–61], helium [62, 63], and other first-row elements [26–29, 32]. The Coulomb interactions are described via pair density matrices [64, 65], which are evaluated at an imaginary time interval of $[512 \text{ Hartree (Ha)}]^{-1}$. The nodal restriction is enforced in much smaller steps of $[8192 \text{ Ha}]^{-1}$.

For our DFT-MD simulations, we choose the hardest available projected augmented wave (PAW) pseudopotentials [66] for boron with core radii of 1.1 Bohr and frozen $1s^2$ electron, as provided in the Vienna *Ab initio* Simulation Package (VASP) [67]. We use the Perdew-Burke-Ernzerhof (PBE) [68] functional to describe the electronic exchange-correlation interactions, which has been shown to be superior to the local density approximation in studies of boron at low temperature [69]. We choose a large cutoff energy of 2000 eV for the plane-wave basis, and we use the Γ point to sample the Brillouin zone. The simulations are carried out in the *NVT* ensemble with a temperature-dependent time step of 0.05–0.55 fs, chosen to ensure reasonable conservation of energy. The temperature is regulated by a Nosé thermostat [70]. Each MD trajectory typically consists of 5000 steps to ensure that the system has reached equilibrium and to establish convergence of the energies and pressures. DFT-MD energies from VASP reported in this study are shifted by -24.596 Ha/B , the all-electron PBE energy of a single boron atom determined with OPIUM [71], in order to establish a consistent comparison with the all-electron PIMC energies.

Our PIMC calculations are performed at temperatures from $5.05 \times 10^5 \text{ K}$ to $5.17 \times 10^8 \text{ K}$ and densities ranging from 0.1- to 20-times the ambient density ρ_0 ($\sim 2.46 \text{ g/cm}^3$ based on that of the α phase [72]). We conduct DFT-MD simulations at temperatures between $5.05 \times 10^4 \text{ K}$ and 10^6 K , in order to check the PIMC calculations at the lowest temperatures. Due to limitations in applying the plane-wave basis for orbital expansion at low densities, and limitations in the applicability of the pseudopotentials that freeze $1s^2$ electrons in the core at high densities, we consider a smaller number of densities (ρ_0 – $10\rho_0$) in DFT-MD. These conditions are relevant to the dynamic shock compression experiments we have conducted at the NIF, and span the range in which Kohn-Sham DFT-MD simulations are feasible. All PIMC

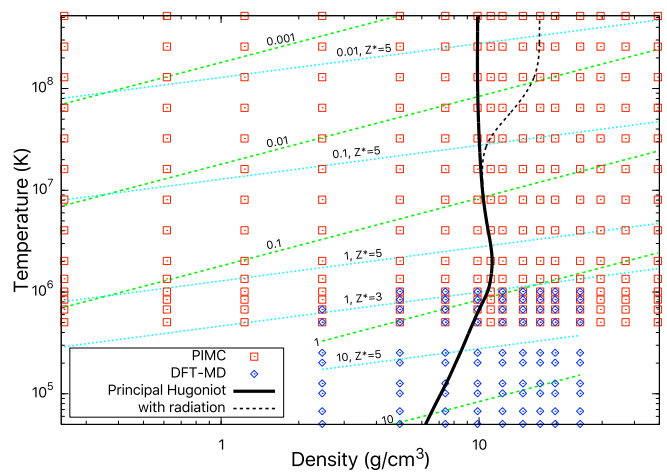


FIG. 1. Temperature-density conditions in our PIMC (red squares) and DFT-MD (blue diamonds) calculations are shown. The black curves depict the computed principal Hugoniot with (dashed) and without (solid) radiation correction [73] to the EOS. The dashed lines in green represent the conditions with different values of the degeneracy parameter, Ψ , and the dotted lines in cyan denote the effective ionic coupling parameter, Γ . The Hugoniot curve is constructed by choosing the initial density to be the same as ρ_0 ($\sim 2.46 \text{ g/cm}^3$).

calculations use 30-atom cubic cells, while in DFT-MD we consider both 30-atom cells and larger cells with 108 and 120 boron atoms to minimize the finite-size errors.

The temperature-density conditions included in this study are shown in Fig. 1, along with contour lines corresponding to the ionic coupling parameter, $\Gamma = (Z^*e)^2 / (ak_B T)$, and the electron degeneracy parameter, $\Psi = T_{\text{Fermi}} / T$, where T_{Fermi} is the Fermi temperature of free electrons, Z^* is the effective ion charge, k_B is the Boltzmann constant, $a = (3/4\pi n)^{1/3}$ is the average ionic distance, and n is the ion number density. Our PIMC and DFT-MD calculations span a wide range of conditions for the boron plasma, including weakly coupled ($\Gamma < 1$) plasmas, as well as collisional, strongly coupled ($\Gamma > 1$) and degenerate ($\Psi > 1$) plasmas. We utilize the simulation data to predict the principal shock Hugoniot profile over a range of pressures spanning 10 to 10^5 megabar (Mbar), as described in Section III B.

B. Shock Hugoniot experiment

An experiment to measure boron's Hugoniot near 50 Mbar was done at the NIF [74] at Lawrence Livermore National Laboratory (shot number N170801), using the impedance-matching technique. As shown in Fig. 2, the target physics package was affixed to the side of a gold hohlraum and comprised a 200- μm -thick diamond ablator, 5- μm -thick gold preheat shield, and a 100- μm -thick diamond impedance-matching standard backing individ-

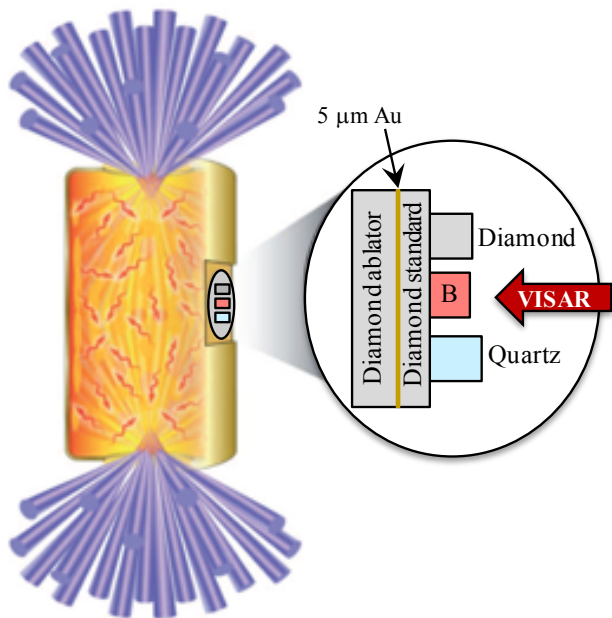


FIG. 2. Target design for the impedance-matching experiment at the NIF.

ual diamond, boron, and quartz samples. The optical-grade chemical vapor deposition diamond was polycrystalline with a density of 3.515 g/cm^3 . The z-cut α -quartz and the boron had densities of 2.65 g/cm^3 and 2.31 g/cm^3 , respectively. 176 laser beams in a 5-ns pulse with a total energy of 827 kJ produced an x-ray bath in the hohlraum with a peak radiation temperature of 250 eV as measured by Dante [75]. The x rays launched a strong, planar and nearly steady shock wave, varying $\pm 3\%$ from its average velocity in the boron, that drove the samples to high pressures and temperatures.

The boron Hugoniot measurement was determined by impedance matching using the inferred shock velocities in the boron sample and diamond standard. Average shock velocities were determined from shock transit times, measured using a line-imaging velocity interferometer system for any reflector (VISAR) [76], and the initial sample thicknesses, measured using a dual confocal microscope. The average velocities were further corrected for shock unsteadiness witnessed *in situ* in the transparent quartz sample [77–79]. The Hugoniot and release for the diamond standard were calculated using a tabular equation of state (LEOS 9061) created from a multiphase model based on DFT-MD and PIMC calculations [80]. The experimental Hugoniot data are given in Table I.

III. RESULTS

A. Equation of state

The first-principles EOS computed with PIMC and DFT-MD calculations are shown in Figs. 3a and b. The

internal energies and pressures we computed using PIMC are consistent with those predicted by the ideal Fermi gas theory and the Debye-Hückel model in the high temperature limit ($> 1.6 \times 10^7 \text{ K}$) where these models are valid. At lower temperatures, ideal Fermi gas theory and Debye-Hückel model predictions become increasingly higher and lower, respectively, than our PIMC values for both internal energy and pressure. This is easily understood due to the increased contribution from electron-electron and electron-ion correlations at lower temperature which render the high-temperature theories inadequate. The PIMC energies and pressures show the same trend as those from our DFT-MD simulations along all the nine isochores between ρ_0 – $10\rho_0$.

The explicit inclusion of electronic shell structures leads to significant differences in the EOS of boron relative to the TF model, in particular at $T \leq 2 \times 10^6 \text{ K}$. In comparison with our first-principles data, the LEOS 50 pressures differ by a variation -16.4% to 7.1%, and the internal energy differences are between -2.0–8.2 Ha/atom, at $T \leq 2.0 \times 10^6 \text{ K}$. These differences lead to significantly different peak compression in the shock Hugoniot curves, as will be discussed in Sec. III B. At high temperatures ($T > 2 \times 10^6 \text{ K}$), the relative differences in energies and pressures are small (between -3.1% and 0.5% in pressure, and between -1% and 6% in internal energy).

With decreasing temperature from 10^6 to $5.05 \times 10^5 \text{ K}$, we find improved agreement between PIMC and DFT-MD results in both internal energy and pressure (Fig. 3c,d). We define a critical temperature of $5.05 \times 10^5 \text{ K}$ corresponding to the temperature above which significant ionization of the boron $1s^2$ core state is expected to render the pseudopotential calculation inaccurate. This critical temperature is lower than what we found recently for carbon in CH (10^6 – $2 \times 10^6 \text{ K}$). This is due to the shallower $1s$ level in boron than in carbon. At the critical temperature, we find good consistency between PIMC and DFT-MD, with differences less than 1.5 Ha/B in energy and less than 5% in pressure.

The larger underestimation in energy and pressure by DFT-MD at higher densities and temperatures can be attributed to the failure of the pseudopotential approximation at these conditions. The significant compression at densities higher than $5\rho_0$ leads to the overlap of the nearby frozen cores, which makes the use of the pseudopotential inaccurate at these conditions. In previous studies, other authors have overcome the failure of the pseudopotentials by constructing all-electron pseudopotentials that maintain accuracy up to higher temperatures and densities.[15, 81] We note that the DFT-MD calculations shown here up to the critical temperature are in good agreement with the all-electron results, and the PIMC calculations agree with the all-electron calculations at the higher temperatures.

TABLE I. Boron Hugoniot data from impedance matching (IM) with a diamond standard. Shock velocities (U_s) at the IM interface were measured *in situ* using VISAR for quartz (Q) and inferred using the nonsteady waves correction for boron (B) and diamond (C). U_s^C and U_s^B were used in the IM analysis to determine the particle velocity (u_p), pressure (P), and density (ρ) on the boron Hugoniot.

| U_s^Q (km/s) | U_s^C (km/s) | U_s^B (km/s) | u_p^B (km/s) | P^B (GPa) | ρ^B (g/cm ³) |
|-------------------|-------------------|-------------------|-------------------|----------------|----------------------------------|
| 55.18 ± 0.25 | 55.25 ± 0.74 | 58.71 ± 0.66 | 41.35 ± 0.82 | 5608 ± 118 | 7.811 ± 0.465 |

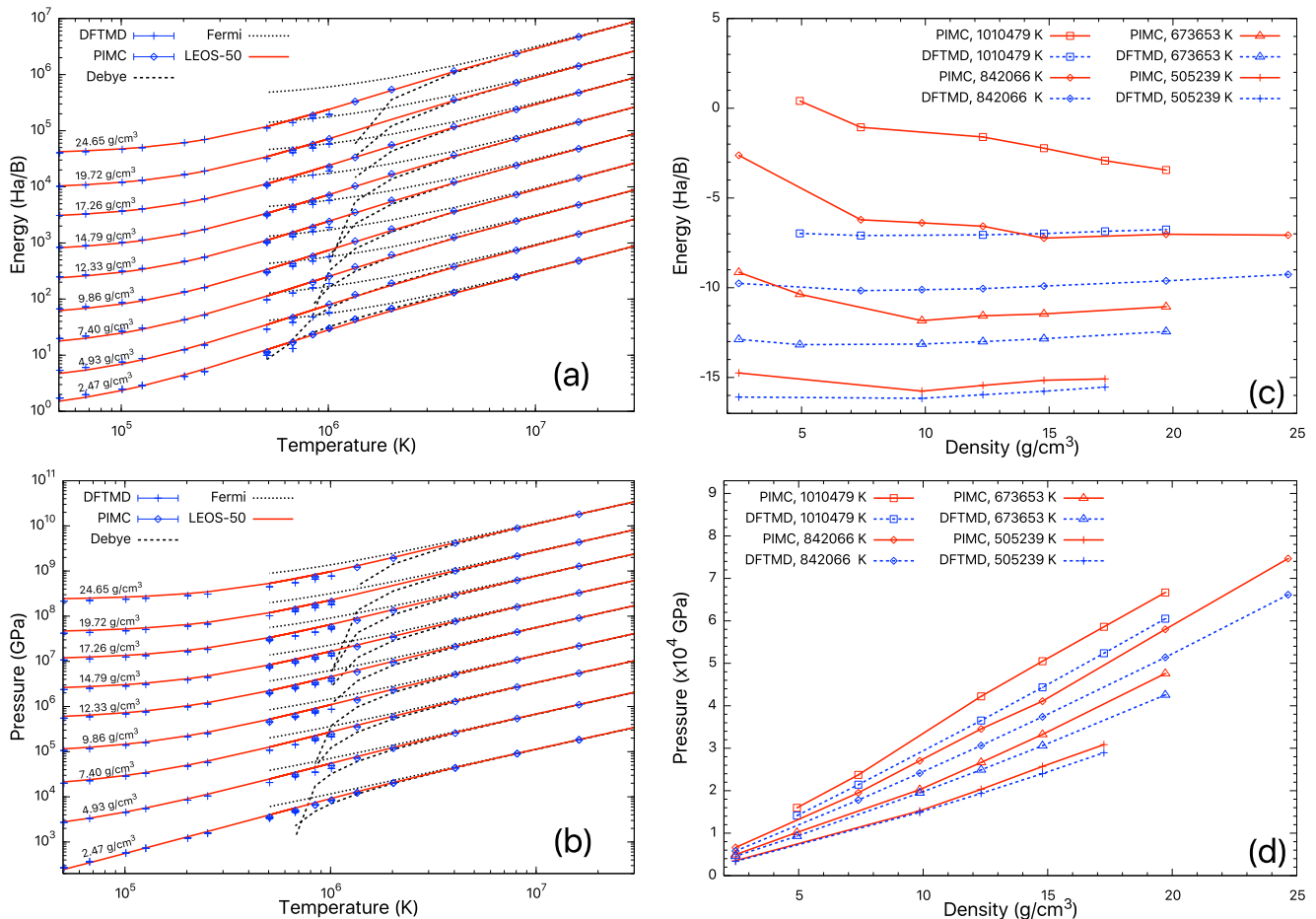


FIG. 3. (a) Energy- and (b) pressure-temperature EOS plots along isochores for boron from our PIMC and DFT-MD simulations. For comparison, the ideal Fermi-gas theory, Debye-Hückel model, and LEOS 50 are also shown. In (a), the LEOS 50 data have been aligned with DFT by setting their energies to be equal at 2.46 g/cm³ and 0 K. Subplots (c) and (d) are the comparison in internal energy and pressure between PIMC and DFT-MD along four isotherms as functions of density. In subplots (a) and (b), results at different isochores have been shifted apart for clarity.

B. Shock compression

During planar shock compression, the locus of the final (shocked) state (E, P, V) is related to the initial (pre-shocked) state (E_0, P_0, V_0) via the Rankine-Hugoniot equation [82]

$$(E - E_0) + \frac{1}{2}(P + P_0)(V - V_0) = 0, \quad (1)$$

where E , P , and V denotes internal energy, pressure, and volume, respectively. Equation 1 allows for determining

the P - V - T Hugoniot conditions with the EOS data in Sec. III A.

We plot the Hugoniot curves thus obtained in a pressure-compression ratio ($P - \rho/\rho_0$, where ρ is the density in the shocked state) and a temperature-pressure ($T - P$) diagram in Fig. 4, and in a $T - \rho$ diagram in Fig. 1. Our EOS based on PIMC calculations predict a maximum compression of 4.6 at 0.85 gigabar pressure and 2.0 million K temperature. In comparison, LEOS 50 and SESAME 2330 models predict boron to be stiffer by

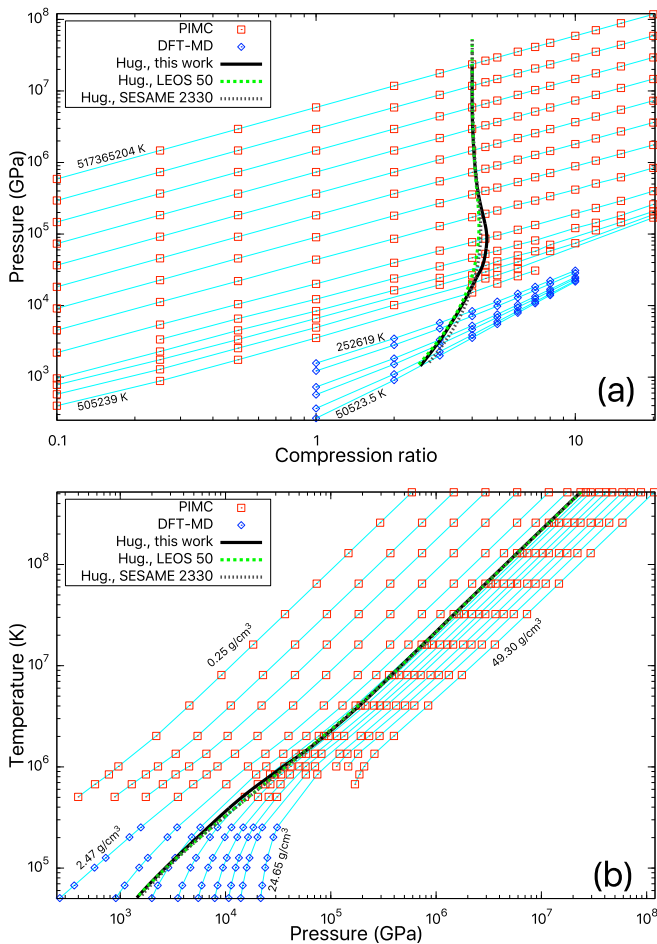


FIG. 4. Boron EOS and shock Hugoniot curves shown in (a) $P - \rho/\rho_0$ and (b) $T - P$ plots. The Hugoniot curves from LEOS 50 and SESAME 2330 are co-plotted for comparison. Cyan-colored curves in panels (a) and (b) denote isotherms and isochores, respectively. The Hugoniot curves are constructed by choosing the initial density to be the same as ρ_0 ($\sim 2.46 \text{ g/cm}^3$).

6.9% and 5.5%, respectively, at the maximum compression. The difference originates from the 1s shell ionization, which increases the compression ratio and is well captured in the PIMC simulations but not in the TF-based LEOS 50 and SESAME 2330 models. A similar deviation has been found for other low- Z systems, such as CH [33, 34]. At lower temperatures, LEOS 50 predictions of the $P - \rho/\rho_0$ relation agree with our DFT-MD findings, while SESAME 2330 predicts boron to be softer by 6-10%. These are related to the specific details in constructing the cold curve and the thermal ionic parts in the EOS models.

The experimental boron Hugoniot data are summarized in Table I and compared with our theoretical predictions in a pressure-density plot (Fig. 5). The measured data point agrees perfectly with predictions by our first-principles calculations and LEOS 50, but the predictions

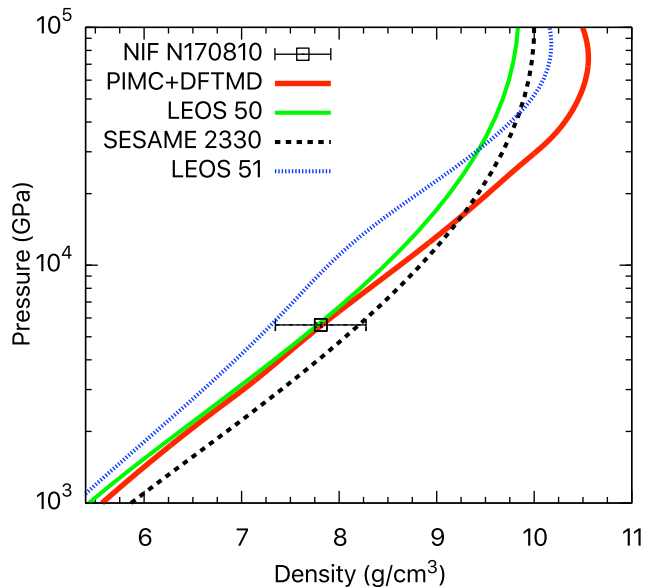


FIG. 5. Comparison of the experimental boron shock Hugoniot result with predictions from our first-principles EOS data and LEOS 50, SESAME 2330, and Purgatorio-based LEOS 51 models. When constructing the Hugoniot curve using the theoretical EOS data, the initial density is set to be the same as the experimental value of 2.31 g/cm^3 (β -boron).

from the Purgatorio-based LEOS 51 and SESAME 2330 models are also consistent with the measurement if the 1σ error bar in density is taken into account.

IV. DISCUSSION

A. Static and dynamic properties of boron plasmas

The EOS and shock compression of warm and hot dense matter can be understood from the atomic and electronic structures. Figure 6 compares the ionic radial distribution function $g(r)$ for boron at selected densities (3-, 5-, and 7-times ρ_0) and temperatures (6.74×10^4 , 1.26×10^5 , and $5.05 \times 10^5 \text{ K}$) from our DFT-MD simulations. At $6.74 \times 10^4 \text{ K}$, the $g(r)$ function shows a peak-valley feature between distances of 1.0–2.0 Å from the nucleus, which is characteristic of a bonding liquid. This feature gradually vanishes as temperature increases, indicating that the system increasingly approaches an ideal gas. However, there is a striking difference of the warm dense matter from the ideal gas in that the atoms within this matter are partially ionized.

The pressure-driven and thermal ionization processes can be well described by comparing the $N(r)$ functions, which denote the average number of electrons within distance r from each nucleus, with the corresponding profile of the B^{3+} ionization state. $N(r)$ curves that are fully above the profile for B^{3+} are associated with fully occu-

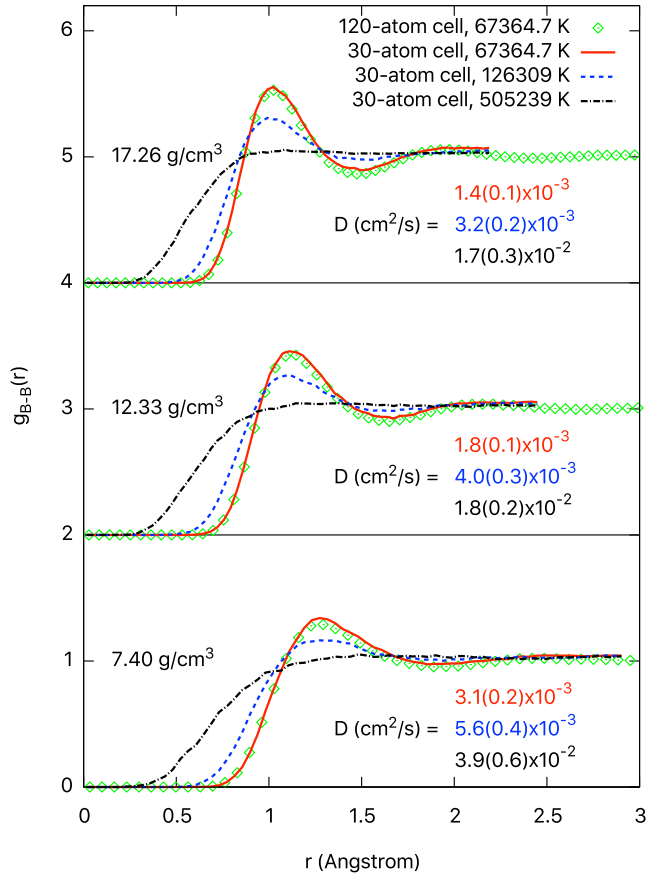


FIG. 6. Nuclear pair correlation function $g(r)$ of boron at three densities and three temperatures. The $g(r)$ curves analyzed based on MD simulations of 120-atom cells at 6736.47 K are co-plotted for comparison. Curves at different densities have been off set for clarity. The consistency between $g(r)$ of 30- and 120-atom cells show negligible finite size effect in describing the ionic structures. The numbers at the inset of each panel show the values of self diffusivity at the corresponding density. Numbers in parentheses denote the standard error of the corresponding data. Red, blue, and dark-colored texts correspond to temperatures of 6.7×10^4 , 1.3×10^5 , and 5.1×10^5 K, respectively.

pied K shells, while those falling below indicate K -shell ionization. The results at $0.1 \times$, $1.0 \times$, $4.0 \times$, and $20 \times \rho_0$ from our PIMC calculations are shown in Fig. 7. We find no observable ionization of the $1s$ states for $T < 0.5 \times 10^6$ K at $\rho > \rho_0$, which validates the use of the pseudopotential with a helium core in our DFT-MD simulations in these temperature and density conditions. As T exceeds 0.5×10^6 K, $1s$ electrons are excited and thus contribute to the total pressure and energy of the system, which explains why both quantities are underestimated in DFT-MD, as has been shown in Fig. 3 and discussed in Sec. III A.

The $N(r)$ results also show that it requires higher temperatures for the K shell to reach the same degree of ionization at higher densities and that the same temperature

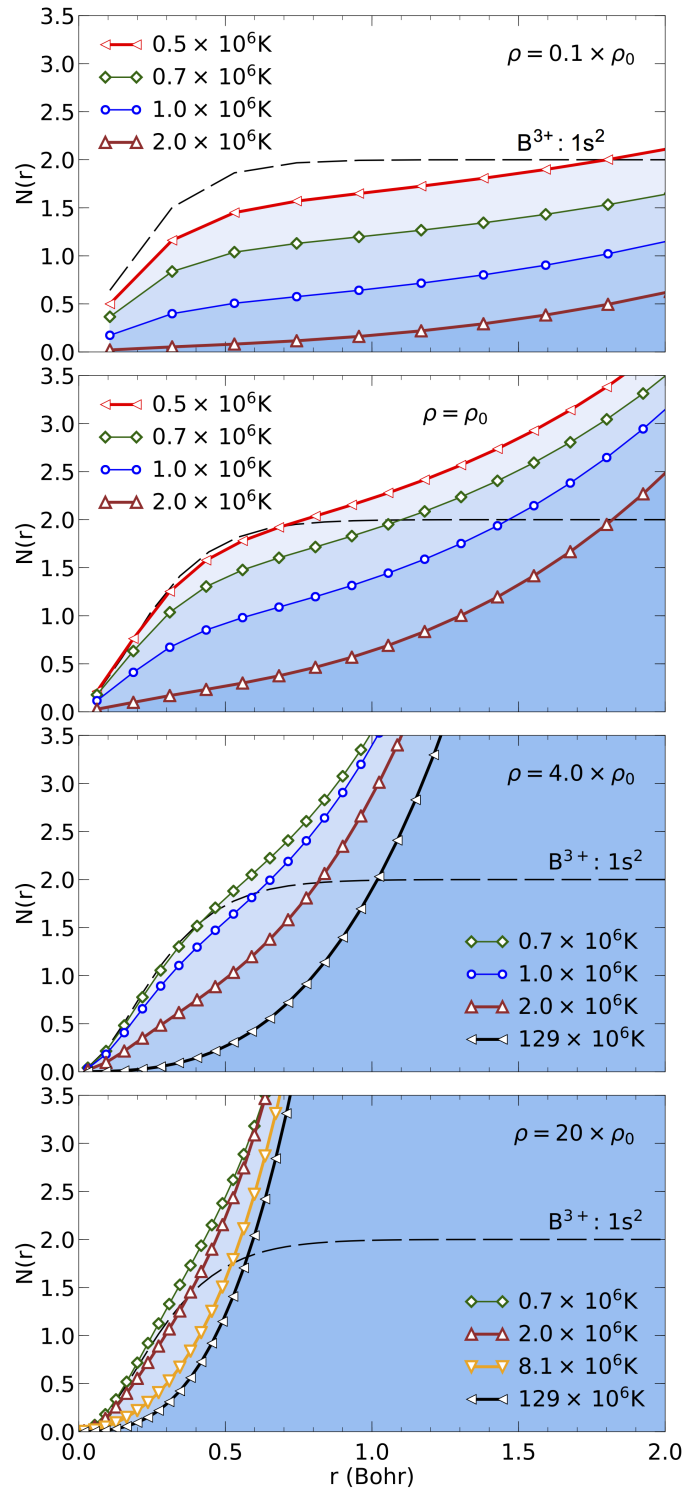


FIG. 7. The average number of electrons around each nucleus at different densities and a series of temperatures. ρ_0 is 2.465 g/cm^3 . The long dashed curve denotes the corresponding profile of the B^{3+} ionization state calculated with GAMESS [83].

change is associated with larger degrees of K shell ionization at lower densities. Previous generalized chemical models [42] showed increasing fraction of B^{2+} particles at $T > 3.5 \times 10^4$ K and negligible K shell ionization within the complete temperature range (up to 4.2×10^4 K) of their study for low-density (0.094 g/cm^3) boron plasmas, which remarkably agree with our findings here based on first-principles calculations.

In order to elucidate the physical origin of these observations, we compare the temperature dependence of the $1s$ binding energy E_b^{1s} with the chemical potential E_{CP} along four different isochores between $0.1\times$ and $20\times\rho_0$. The results are obtained using the Purgatorio method [12, 13] and are summarized in Fig. 8. As density increases, E_b^{1s} rises closer to the continuum level ($E=0$). E_{CP} also increases with increasing density, and in fact increases faster than E_b^{1s} . As a result, the Fermi occupation number of the $1s$ state actually increases with increasing density. At the temperature at which the E_b^{1s} and E_{CP} curves intersect, the $1s$ energy level has a Fermi occupation number of $1/2$. The dash-dotted curves in Fig. 8 plot the chemical potential minus $5k_B T$. The $1s$ level will have a Fermi occupation number of just 0.67% below full occupancy at the temperature at which these curves intersect the corresponding $1s$ energy levels. This intersection therefore indicates the critical temperature at which the $1s$ level starts to ionize. This intersection point shifts to higher temperature with increasing density, indicating that the ionization temperature increases with density, even though the $1s$ binding energy itself decreases. This accounts for the higher temperatures that are required for the K shell to reach the same degree of ionization at higher densities, as observed in Fig. 7. Purgatorio calculations of the K -shell occupation refines the critical temperature to 3.2×10^5 – 3.6×10^5 K at densities between ρ_0 – $4\rho_0$. We have also compared the Purgatorio results to that of DFT simulations of boron on a face-centered cubic lattice using a dual-projector Optimized Norm-Conserving Vanderbilt (ONCV) [84, 85] pseudopotential with core radius equaling 0.8 Bohr. The ONCV and the Purgatorio results on chemical potential, K shell ionization energies, and K shell occupation are in good agreement with each other.

The above findings about ionization are also consistent with the upshifting in energy, decreasing in magnitude, and expanding in width of the peak in heat capacity (Fig. 9) as density increases. The peaks originate from the excitation of $1s$ electrons of boron and appear at lower temperatures than that of carbon in CH with comparable densities [34]. This is because the K shell of boron is shallower than that of carbon.

We also estimate the self diffusion coefficient D for boron using the mean square displacement and the Einstein relation. We obtained values of D that range between 8×10^{-4} and $0.05 \text{ cm}^2/\text{s}$ at the temperatures (5×10^4 – 5×10^5 K) and densities (ρ_0 – $10\rho_0$) that we performed DFT-MD simulations. We find the values of D (some shown in Fig. 6) monotonically increase with tem-

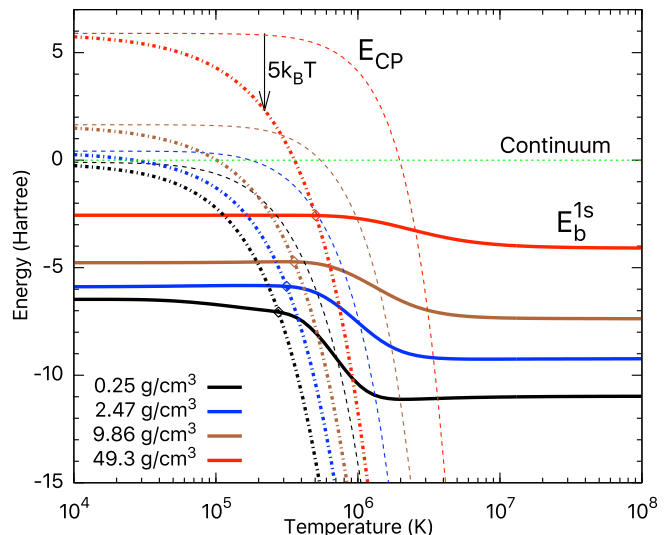


FIG. 8. Comparison of the $1s$ binding energy E_b^{1s} (solid curves) with the chemical potential E_{CP} (thin dashed curves) as functions of temperature at four densities. The data are obtained using the Purgatorio method. The dash-dotted curves represent $E_{CP} - 5k_B T$. The diamonds indicate the points at which the $1s$ level starts to be ionized (by 0.67%).

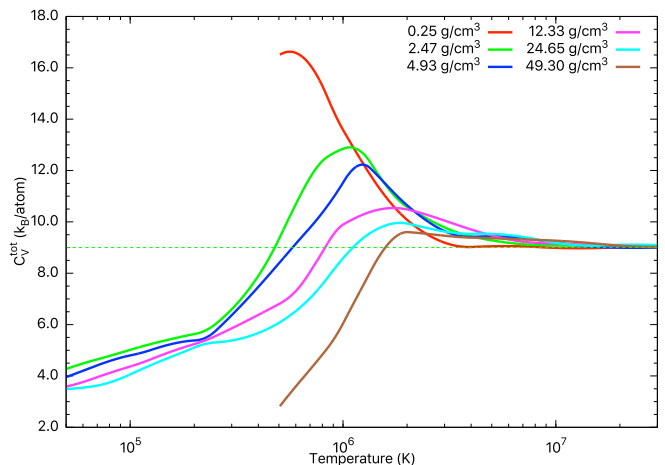


FIG. 9. Total heat capacity $C_V^{tot} = (\partial E / \partial T)|_V$ of boron obtained from our DFT-MD and PIMC data along several isochores. All curves converge to the ideal-gas limit of $9k_B/\text{atom}$ at high temperature.

perature and the specific volume. This is similar to what have been found for the diffusion of hydrogen in asymmetric binary ionic mixtures [86] and deuterium-tritium mixtures [87].

We note that accurate DFT-MD simulations of transport properties, such as diffusivity and viscosity, of one component plasmas across a wide coupling regime are useful because of the potential breakdown of laws for ordinary condensed matter (e.g., the Arrhenius relation) [88]. These studies also build the base for estimat-

ing the corresponding properties of mixtures [87] which, together with EOS approximations (e.g., average-atom or linear mixing approximation [33, 34]), are important in characterizing multi-component plasmas. However, such simulations require much more extended length of the MD trajectories and range of temperatures and densities in the more strongly-coupled regime, which are beyond the scope of this work.

B. PDXP performance sensitivity to EOS

In Ref. 2, a 1D ARES [89, 90] model for the PDXP platform with GDP capsules was developed to match the x-ray bang time and yield of N160920-003, N160920-005, and N160921-001. While we anticipate that changing the ablator in these experiments would necessitate recalibration of this model to match the performance of a new material, this model nonetheless offers a reasonable starting point for examining EOS sensitivity. The capsule in N160920-005 consisted of a 18 μm thick GDP shell with an outer diameter of 2.95 mm, filled with 8-bar of D_2 gas and a trace amount of argon as a spectroscopic tracer. The implosion was driven by a 1.8 ns square pulse corresponding to a peak intensity of about $9.7 \times 10^{14} \text{ W/cm}^2$. The model developed in Ref. 2 incorporates a multiplier on the energy delivered to the capsule, a flux limiter on the electron thermal conduction to account for inadequacies in the assumption of the diffusion model for heat transport, and a multiplier on the mass diffusion coefficient that is used to calibrate the multi-component Navier-Stokes model for mixing of the capsule ablator into the deuterium fuel. The authors also modify the laser intensity used in the 1D simulations to account for geometric losses based on 2D ARES simulations. As discussed in Sec. III A, our *ab initio* simulations yield pressures that differ by up to 20% from the existing LEOS 50 table. The largest variations occur at temperatures between about 1×10^5 and $5 \times 10^6 \text{ K}$, as shown in Fig. 3. In this regime, the electron thermal pressure is the largest contribution to the total pressure. We have therefore performed 1D ARES simulations using the LEOS 50 table with pressure multipliers of 0.8, 1.0, and 1.2 as a means of estimating the EOS sensitivity in a PDXP capsule using a boron ablator.

Because boron is substantially more dense than GDP (2.465 g/cm^3 compared to 1.046 g/cm^3), and because the higher tensile strength should allow for a thinner shell, we have chosen a thickness of 6 μm for the boron capsules. The results of the EOS sensitivity study are shown in Table II. We find that the variations in pressure considered here result in yield variations of -35% to +48%. Higher ablator pressures result in higher gas areal density and higher convergence at burn time for very similar ion temperatures, thus the impact on yield is generated primarily via higher compression of the D_2 gas as the pressure in the ablator increases. The shell areal density at the time of peak neutron production is also impacted

by the pressure multiplier.

For reference, the results from the model calculations in Ref. 2 are also listed in Table II. We find that the 1D ARES model predicts lower gas and much lower shell areal density at peak burn time for the boron ablator compared to GDP. This is because a larger portion of the thinner boron shell is ablated, allowing behavior more like a true exploding pusher than the thicker GDP ablator. The GDP design has a substantial amount of unablated plastic, leading to a lower implosion velocity, higher convergence, and lower ion temperatures relative to the boron ablator. The first-principles calculations and experiments performed in this study will be used to generate a new EOS for B, which will be applied in future 2D calculations of the PDXP platform with a boron ablator.

V. CONCLUSIONS

In this work, we present first-principles EOS results of boron using PIMC and DFT-MD simulations from temperatures of $5 \times 10^4 \text{ K}$ to $5.2 \times 10^8 \text{ K}$. PIMC and DFT-MD cross-validates each other by showing remarkable consistency in the EOS ($<1.5 \text{ Ha/B}$ in total internal energy and $<5\%$ in total pressure) at $5 \times 10^5 \text{ K}$. Our benchmark-quality EOS for boron provides an important base for future theoretical investigations of plasmas with boron.

We measured the boron Hugoniot at the highest pressure to date ($56.1 \pm 1.2 \text{ Mbar}$) in a dynamic compression experiment at NIF. The result shows excellent agreement with that obtained from the first-principles EOS data. In addition, our calculations predict a maximum compression of 4.6, which originates from K shell ionization and is slightly larger than those predicted by TF models LEOS 50 and SESAME 2330.

We investigated the PDXP performance sensitivity to the EOS with a 1D hydrodynamic model. The simulation results show that variations in pressure by -20% and 20% result in neutron yield variations of -35% to +48%, respectively.

ACKNOWLEDGMENTS

This research is supported by the U. S. Department of Energy, grant DE-SC0016248. Computational support was mainly provided by the Blue Waters sustained-petascale computing project (NSF ACI 1640776), which is supported by the National Science Foundation (awards OCI-0725070 and ACI-1238993) and the state of Illinois. Blue Waters is a joint effort of the University of Illinois at Urbana-Champaign and its National Center for Supercomputing Applications. S.Z. is partially supported by the PLS-Postdoctoral Grant of the Lawrence Livermore National Laboratory. This work was in part performed under the auspices of the U.S. Department of Energy by Lawrence Livermore National Laboratory under Contract No. DE-AC52-07NA27344.

TABLE II. Polar direct-drive exploding pushers performance sensitivity to pressure change in boron EOS (based on LEOS 50). Corresponding data based on a GDP model are also shown for comparison.

| Pressure Multiplier | Neutron Yield | Xray Bang Time (ns) | Gas Areal Density (mg/cm ²) | Shell Areal Density (mg/cm ²) | Convergence Ratio | Burn-averaged Ion Temperature (keV) |
|-----------------------|-----------------------|---------------------|---|---|-------------------|-------------------------------------|
| 0.8 | 1.72×10^{13} | 2.22 | 5.98 | 3.11 | 4.79 | 20.48 |
| 1 | 2.68×10^{13} | 2.24 | 7.54 | 3.82 | 5.61 | 22.11 |
| 1.2 | 3.96×10^{13} | 2.28 | 10.5 | 5.06 | 6.96 | 21.73 |
| GDP model from Ref. 2 | 1.97×10^{13} | 3.02 | 17.7 | 23.8 | 12.39 | 7.11 |

- [1] M. G. Johnson, D. T. Casey, M. Hohenberger, A. B. Zylstra, A. Bacher, C. R. Brune, R. M. Bionta, R. S. Craxton, C. L. Ellison, M. Farrell, J. A. Frenje, W. Garbett, E. M. Garcia, G. P. Grim, E. Hartoumi, R. Hatarik, H. W. Herrmann, M. Hohensee, D. M. Holunga, M. Hoppe, M. Jackson, N. Kabadi, S. F. Khan, J. D. Kilkenny, T. R. Kohut, B. Lahmann, H. P. Le, C. K. Li, L. Masse, P. W. McKenty, D. P. McNabb, A. Nikroo, T. G. Parham, C. E. Parker, R. D. Petrasso, J. Pino, B. Remington, N. G. Rice, H. G. Rinderknecht, M. J. Rosenberg, J. Sanchez, D. B. Sayre, M. E. Schoff, C. M. Shulberg, F. H. Sguin, H. Sio, Z. B. Walters, and H. D. Whitley, *Phys. Plasmas* **25**, 056303 (2018).
- [2] C. L. Ellison, H. D. Whitley, C. R. D. Brown, W. Garbett, H. Le, M. B. Schneider, Z. B. Walters, H. Chen, J. I. Castor, R. S. Craxton, M. Gatu Johnson, E. M. Garcia, F. R. Graziani, J. C. Hayes, G. E. Kemp, C. M. Krauland, P. W. McKenty, B. Lahmann, J. E. Pino, M. S. Rubery, H. A. Scott, and R. Shepherd, submitted to *Physics of Plasmas*.
- [3] Probing the Physics of Burning DT Capsules Using Gamma-ray Diagnostics, A. C. Hayes-Sterbenz, G. M. Hale, G. Jungman, and M. W. Park, LA-UR-15-20627.
- [4] B. Hammel, S. Haan, D. Clark, M. Edwards, S. Langer, M. Marinak, M. Patel, J. Salmonson, and H. Scott, *High Energy Density Physics* **6**, 171 (2010), iCHED 2009 - 2nd International Conference on High Energy Density Physics.
- [5] H. F. Robey, J. D. Moody, P. M. Celliers, J. S. Ross, J. Ralph, S. Le Pape, L. Berzak Hopkins, T. Parham, J. Sater, E. R. Mapoles, D. M. Holunga, C. F. Walters, B. J. Haid, B. J. Koziolowski, R. J. Dylla-Spears, K. G. Krauter, G. Frieders, G. Ross, M. W. Bowers, D. J. Strozzi, B. E. Yoxall, A. V. Hamza, B. Dzenitis, S. D. Bhandarkar, B. Young, B. M. Van Wierterghem, L. J. Atherton, O. L. Landen, M. J. Edwards, and T. R. Boehly, *Phys. Rev. Lett.* **111**, 065003 (2013).
- [6] V. A. Smalyuk, D. T. Casey, D. S. Clark, M. J. Edwards, S. W. Haan, A. Hamza, D. E. Hoover, W. W. Hsing, O. Hurricane, J. D. Kilkenny, J. Kroll, O. L. Landen, A. Moore, A. Nikroo, L. Peterson, K. Raman, B. A. Remington, H. F. Robey, S. V. Weber, and K. Widmann, *Phys. Rev. Lett.* **112**, 185003 (2014).
- [7] S. X. Hu, V. N. Goncharov, T. R. Boehly, R. L. McCrory, S. Skupsky, L. A. Collins, J. D. Kress, and B. Militzer, *Phys. Plasmas* **22**, 056304 (2015).
- [8] S. X. Hu, L. A. Collins, V. N. Goncharov, J. D. Kress, R. L. McCrory, and S. Skupsky, *Phys. Rev. E* **92**, 043104 (2015).
- [9] R. M. More, K. H. Warren, D. A. Young, and G. B. Zimmerman, *Phys. Fluids* **31**, 3059 (1988).
- [10] D. A. Young and E. M. Corey, *J. Appl. Phys.* **78**, 3748 (1995).
- [11] D. A. Liberman, *Phys. Rev. B* **20**, 4981 (1979).
- [12] B. Wilson, V. Sonnad, P. Sterne, and W. Isaacs, *J. Quant. Spectrosc. Radiat. Transfer* **99**, 658 (2006).
- [13] P. Sterne, S. Hansen, B. Wilson, and W. Isaacs, *High Energy Density Physics* **3**, 278 (2007), radiative Properties of Hot Dense Matter.
- [14] F. Lambert, J. Cl  rouin, and G. Z  rah, *Phys. Rev. E* **73**, 016403 (2006).
- [15] J.-F. Danel, L. Kazandjian, and G. Zrah, *Phys. Plasmas* **19**, 122712 (2012).
- [16] S. Zhang, H. Wang, W. Kang, P. Zhang, and X. T. He, *Phys. Plasmas* **23**, 042707 (2016).
- [17] F. J. Rogers, *Astrophys. J.* **310**, 723 (1986).
- [18] F. J. Rogers, *Equation of State in Astrophysics*, IAU Colloquium 147, pp. 16-42, eds. G. Chabrier & E. Schatzman (Cambridge Univ. Press, Cambridge, 1994).
- [19] F. J. Rogers, F. J. Swenson, and C. A. Iglesias, *Astrophys. J.* **456**, 902 (1996).
- [20] E. Pollock and D. Ceperley, *Phys. Rev. B* **30**, 2555 (1984).
- [21] E. L. Pollock, *Comput. Phys. Commun.* **52**, 49 (1988).
- [22] D. M. Ceperley, *Rev. Mod. Phys.* **67**, 279 (1995).
- [23] D. M. Ceperley, in *Monte Carlo and Molecular Dynamics of Condensed Matter Systems* (Editrice Compositori, Bologna, Italy, 1996) p. 443.
- [24] B. Militzer and K. P. Driver, *Phys. Rev. Lett.* **115**, 176403 (2015).
- [25] C. Pierleoni, D. M. Ceperley, B. Bernu, and W. R. Magro, *Phys. Rev. Lett.* **73**, 2145 (1994).
- [26] K. P. Driver and B. Militzer, *Phys. Rev. Lett.* **108**, 115502 (2012).
- [27] K. P. Driver and B. Militzer, *Phys. Rev. B* **93**, 064101 (2016).
- [28] K. P. Driver, F. Soubiran, S. Zhang, and B. Militzer, *J. Chem. Phys.* **143**, 164507 (2015).
- [29] K. P. Driver and B. Militzer, *Phys. Rev. B* **91**, 045103 (2015).
- [30] S. Zhang, K. P. Driver, F. Soubiran, and B. Militzer, *High Energ. Dens. Phys.* **21**, 16 (2016).
- [31] S. Zhang, K. P. Driver, F. Soubiran, and B. Militzer, *J. Chem. Phys.* **146**, 074505 (2017).
- [32] K. P. Driver and B. Militzer, *Phys. Rev. E* **95**, 043205 (2017).

- [33] S. Zhang, K. P. Driver, F. Soubiran, and B. Militzer, *Phys. Rev. E* **96**, 013204 (2017).
- [34] S. Zhang, B. Militzer, L. X. Benedict, F. Soubiran, P. A. Sterne, and K. P. Driver, *J. Chem. Phys.* **148**, 102318 (2018).
- [35] A. Masago, K. Shirai, and H. Katayama-Yoshida, *Phys. Rev. B* **73**, 104102 (2006).
- [36] S. Shang, Y. Wang, R. Arroyave, and Z.-K. Liu, *Phys. Rev. B* **75**, 092101 (2007).
- [37] T. Ogitsu, E. Schwegler, and G. Galli, *Chem. Rev.* **113**, 3425 (2013).
- [38] A. R. Oganov, J. Chen, C. Gatti, Y. Ma, Y. Ma, C. W. Glass, Z. Liu, T. Yu, O. O. Kurakevych, and V. L. Solozhenko, *Nature* **457**, 863 (2009).
- [39] N. Vast, S. Bernard, and G. Zerah, *Phys. Rev. B* **52**, 4123 (1995).
- [40] J. Cl  rouin, P. Renaudin, and P. Noiret, *Phys. Rev. E* **77**, 026409 (2008).
- [41] D. L. Price, A. Alatas, L. Hennet, N. Jakse, S. Krishnan, A. Pasturel, I. Pozdnyakova, M.-L. Saboungi, A. Said, R. Scheunemann, W. Schirmacher, and H. Sinn, *Phys. Rev. B* **79**, 134201 (2009).
- [42] E. M. Apfelbaum, *Contrib. Plasm. Phys.* **53**, 317 (2013).
- [43] J. Cl  rouin, P. Noiret, P. Blottiau, V. Recoules, B. Siberchicot, P. Renaudin, C. Blancard, G. Faussurier, B. Holst, and C. E. Starrett, *Phys. Plasmas* **19**, 082702 (2012).
- [44] J. Cl  rouin, C. Starrett, G. Faussurier, C. Blancard, P. Noiret, and P. Renaudin, *Phys. Rev. E* **82**, 046402 (2010).
- [45] W. Johnson, C. Guet, and G. Bertsch, *J. Quant. Spectrosc. Radiat. Transfer* **99**, 327 (2006).
- [46] C. Blancard and G. Faussurier, *Phys. Rev. E* **69**, 016409 (2004).
- [47] G. Faussurier, C. Blancard, P. Coss, and P. Renaudin, *Phys. Plasmas* **17**, 052707 (2010).
- [48] S. Kuhlbrodt, B. Holst, and R. Redmer, *Contrib. Plasm. Phys.* **45**, 73 (2005).
- [49] LASL Shock Hugoniot Data, edited by S. P. Marsh (University of California Press, Berkeley, 1980).
- [50] S. Le Pape, A. A. Correa, C. Fortmann, P. Neumayer, T. D  ppner, P. Davis, T. Ma, L. Divol, K.-U. Plagemann, E. Schwegler, R. Redmer, and S. Glenzer, *New Journal of Physics* **15**, 085011 (2013).
- [51] S. P. Lyon and J. D. Johnson, eds., *SESAME: The Los Alamos National Laboratory Equation of State Database* (Group T-1, Report No. LA-UR-92-3407, 1992).
- [52] B. Militzer, Ph.D. Thesis, University of Illinois at Urbana-Champaign (2000).
- [53] D. M. Ceperley, *J. Stat. Phys.* **63**, 1237 (1991).
- [54] W. R. Magro, D. M. Ceperley, C. Pierleoni, and B. Bernu, *Phys. Rev. Lett.* **76**, 1240 (1996).
- [55] B. Militzer and D. M. Ceperley, *Phys. Rev. E* **63**, 066404 (2001).
- [56] B. Militzer, D. M. Ceperley, J. D. Kress, J. D. Johnson, L. A. Collins, and S. Mazevet, *Phys. Rev. Lett.* **87**, 275502 (2001).
- [57] S. X. Hu, B. Militzer, V. N. Goncharov, and S. Skupsky, *Phys. Rev. Lett.* **104**, 235003 (2010).
- [58] B. Militzer and D. M. Ceperley, *Phys. Rev. Lett.* **85**, 1890 (2000).
- [59] S. X. Hu, B. Militzer, V. N. Goncharov, and S. Skupsky, *Phys. Rev. B* **84**, 224109 (2011).
- [60] B. Militzer, W. Magro, and D. Ceperley, *Contrib. Plasm. Phys.* **39**, 151 (1999).
- [61] B. Militzer and R. L. Graham, *J. Phys. Chem. Solids* **67**, 2136 (2006).
- [62] B. Militzer, *Phys. Rev. Lett.* **97**, 175501 (2006).
- [63] B. Militzer, *J. Low Temp. Phys.* **139**, 739 (2005).
- [64] V. Natoli and D. M. Ceperley, *J. Comp. Phys.* **117**, 171 (1995).
- [65] B. Militzer, *Comput. Phys. Commun.* **204**, 88 (2016).
- [66] P. E. Bl  chl, O. Jepsen, and O. K. Andersen, *Phys. Rev. B* **49**, 16223 (1994).
- [67] G. Kresse and J. Furthm  ller, *Phys. Rev. B* **54**, 11169 (1996).
- [68] J. P. Perdew, K. Burke, and M. Ernzerhof, *Phys. Rev. Lett.* **77**, 3865 (1996).
- [69] M. Widom and M. Mihalkovi  , *Phys. Rev. B* **77**, 064113 (2008).
- [70] S. Nos  , *J. Chem. Phys.* **81**, 511 (1984).
- [71] See <http://opium.sourceforge.net> for information about the OPIUM code.
- [72] G. Will and B. Kiefer, *Zeitschrift fr anorganische und allgemeine Chemie* **627**, 2100 (2001).
- [73] The radiation correction was added to our first-principles EOS by considering an ideal black body scenario. Details about the way of adding this correction have been shown in our previous work (Ref. 31). In comparison with electronic relativistic effects, the radiation correction becomes evident along the Hugoniot curve at a lower temperature; whereas in both cases the compression ratio approaches the limit of 7 at high temperature.
- [74] E. I. Moses, R. N. Boyd, B. A. Remington, C. J. Keane, and R. Al-Ayat, *Phys. Plasmas* **16**, 041006 (2009).
- [75] E. L. Dewald, K. M. Campbell, R. E. Turner, J. P. Holder, O. L. Landen, S. H. Glenzer, R. L. Kauffman, L. J. Suter, M. Landon, M. Rhodes, and D. Lee, *Review of Scientific Instruments* **75**, 3759 (2004).
- [76] P. M. Celliers, D. K. Bradley, G. W. Collins, D. G. Hicks, T. R. Boehly, and W. J. Armstrong, *Rev. Sci. Instrum.* **75**, 4916 (2004).
- [77] D. E. Fratanduono, D. H. Munro, P. M. Celliers, and G. W. Collins, *J. Appl. Phys.* **116**, 033517 (2014).
- [78] M. C. Gregor, D. E. Fratanduono, C. A. McCoy, D. N. Polsin, A. Sorce, J. R. Rygg, G. W. Collins, T. Braun, P. M. Celliers, J. H. Eggert, D. D. Meyerhofer, and T. R. Boehly, *Phys. Rev. B* **95**, 144114 (2017).
- [79] D. E. Fratanduono, P. M. Celliers, D. G. Braun, P. A. Sterne, S. Hamel, A. Shamp, E. Zurek, K. J. Wu, A. E. Lazicki, M. Millot, and G. W. Collins, *Phys. Rev. B* **94**, 184107 (2016).
- [80] L. X. Benedict, K. P. Driver, S. Hamel, B. Militzer, T. Qi, A. A. Correa, A. Saul, and E. Schwegler, *Phys. Rev. B* **89**, 224109 (2014).
- [81] S. Mazevet, F. Lambert, F. Bottin, G. Z  rah, and J. Cl  rouin, *Phys. Rev. E* **75**, 056404 (2007).
- [82] M. A. Meyers, *Dynamic Behavior of Materials* (Wiley, New York, 1994).
- [83] See <http://www.msg.ameslab.gov/games/> for information about the GAMESS code.
- [84] D. R. Hamann, *Phys. Rev. B* **88**, 085117 (2013).
- [85] D. R. Hamann, *Phys. Rev. B* **95**, 239906 (2017).
- [86] H. D. Whitley, W. E. Alley, W. H. Cabot, J. I. Castor, J. Nilsen, and H. E. DeWitt, *Contributions to Plasma Physics* **55**, 413 (2015).
- [87] J. D. Kress, J. S. Cohen, D. A. Horner, F. Lambert, and L. A. Collins, *Phys. Rev. E* **82**, 036404 (2010).

- [88] J. Daligault, Phys. Rev. Lett. **96**, 065003 (2006).
- [89] R. M. Darlington, T. L. McAbee, and G. Rodrigue, Comput. Phys. Commun. **135**, 58 (2001).
- [90] B. E. Morgan and J. A. Greenough, Shock Waves **26**, 355 (2016).